Charge Carrier Dynamics in Co-evaporated $MAPbI_3$ with a Gradient in Composition

Zhao, Jiashang; Li, Jia; Liu, Xiaohui; Bannenberg, Lars J.; Bruno, Annalisa; Savenije, Tom J.

DOI
10.1021/acsaem.2c00664

Publication date
2022

Document Version
Final published version

Published in
ACS Applied Energy Materials

Citation (APA)
Zhao, J., Li, J., Liu, X., Bannenberg, L. J., Bruno, A., & Savenije, T. J. (2022). Charge Carrier Dynamics in Co-evaporated $MAPbI_3$ with a Gradient in Composition. *ACS Applied Energy Materials*, *5*(6), 7049-7055. https://doi.org/10.1021/acsaem.2c00664

ACS APPLIED ENERGY MATERIALS

www.acsaem.org Article

Charge Carrier Dynamics in Co-evaporated $MAPbI_3$ with a Gradient in Composition

Jiashang Zhao, Jia Li, Xiaohui Liu, Lars J. Bannenberg, Annalisa Bruno,* and Tom J. Savenije*

Cite This: *ACS Appl. Energy Mater.* 2022, 5, 7049−7055

Read Online

ACCESS | Metrics & More | Article Recommendations | Supporting Information

ABSTRACT: Co-evaporation of metal halide perovskites by thermal evaporation is an attractive method since it does not require harmful solvents and enables precise control of the film thickness. Furthermore, the ability to manipulate the Fermi level allows the formation of a graded homojunction, providing interesting opportunities to improve the charge carrier collection efficiency. However, little is known about how these properties affect the charge carrier dynamics. In this work, the structural and optoelectronic properties of co-evaporated $MAPbI_3$ films varying in thickness (100, 400, and 750 nm) with a gradient in composition are analyzed. The X-ray diffraction patterns show that excess PbI_2 is only present in the thick layers. From X-ray photoelectron spectroscopy depth analysis, the I/Pb atomic ratio indicates methylammonium iodide deficiencies that become more prominent with thicker films, resulting in differently n-doped regions across the thick $MAPbI_3$ films. We suggest that due to these differently n-doped regimes, an internal electric field is formed. Side-selective time-resolved microwave photo conductivity measurements show an elongation of the charge carrier lifetimes on increasing thickness. These observations can be explained by the fact that excess carriers separate under the influence of the electric field, preventing rapid decay in the thick films.

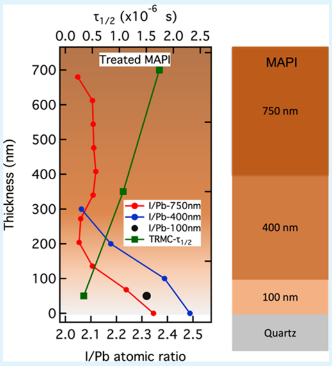

KEYWORDS: *metal halide perovskites, time-resolved microwave conductivity, physical vapor deposition, co-evaporation, charge carrier dynamics*

INTRODUCTION

With unprecedented progress, metal halide perovskite (MHP)-based solar cells have reached power conversion efficiencies (PCEs) of over 25% and are the most promising candidates for next-generation solar cells.[1−6] These remarkable developments are attributed to their intrinsic properties such as high absorption coefficients, relatively high charge carrier mobilities, and long lifetimes as well as low densities of electronically active trap states.[1,7,8] At the same time, MHPs are also emerging in other applications, such as X-ray detectors, light-emitting diodes, field effect transistors, and memory devices.[9−11]

In general, the production of the majority of MHP solar cells is based on solution-processed deposition techniques. However, deposition by thermal co-evaporation under vacuum conditions is an attractive alternative approach to obtain uniform and compact thin films.[12−16] Elimination of solvents is beneficial to the fabrication of tandem solar cells and preservation of the environment. More importantly, this method is scalable and allows precise control of the film thickness, even on textured surfaces.[17,18] The first work published in 2013 using thermal co-evaporation to deposit $MAPbI_{3-x}Cl_x$ reported a PCE of 15.4% for small-area devices.[12] To date, the PCEs of perovskite solar cells based on methylammonium lead iodide ($MAPbI_3$) prepared by co-evaporation reach over 20% in both nip[19−24] and pin[17] configurations on the small-area devices and over 18% on perovskite minimodules.[19,23]

Although deposition of $MAPbI_3$ by wet chemical deposition has been extensively examined, the effects of the co-evaporation processing parameters on the structural and electronic properties of $MAPbI_3$ films are complex and still under investigation. Recently, it was reported that the deposition speed and polarity of the substrate can substantially affect the preferred crystal orientation and morphology of $MAPbI_3$ films.[14] In addition, by tuning the deposition rates of the precursors during the co-evaporation, the crystalline phase of $MAPbI_3$ can be varied from the cubic to the tetragonal phase.[25] On the other hand, Li et al. have shown that another key advantage of co-evaporation is the possibility to customize the active film for different device architectures. Recently, we demonstrated that using $MAPbI_3$ with a gradual change in precursors leading to a gradient in composition, a PCE above 20% can be achieved in a pin configuration.[17] Co-evaporated perovskites have also shown to be very promising in enhancing

Received: March 3, 2022
Accepted: May 6, 2022
Published: May 18, 2022

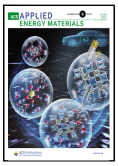

the optoelectronic properties of light-emitting field-effect transistors. Thanks to the reduced ionic motion and absence of tensile stress, it was possible to obtain light emission even at room temperature,[26] which was not possible with spin-coated perovskites.[27]

Herein, we study how the charge carrier dynamics are affected in $MAPbI_3$ films grown with a gradient in composition formed by applying a gradient in pressure during the growth process. We have used a constant source temperature for both precursors, that is, methylammonium iodide (MAI) and PbI_2, which results in a slowly varying background pressure during the deposition.[17] Since the perovskite growth can be largely influenced by the substrate material,[28] in this work, we analyzed $MAPbI_3$ films with different thicknesses deposited on quartz substrates. We performed X-ray diffraction (XRD), scanning electron microscopy (SEM), and X-ray photoinduced spectroscopy (XPS) to investigate the structural properties of the deposited films, with a focus on the I/Pb atomic ratio. It has been previously shown that variations in stoichiometry can affect the Fermi level of the film.[29] Hence, we argue that on Fermi level alignment, an internal field is formed in the 400 and 750 nm $MAPbI_3$ films. This internal field has profound effects on the charge carrier dynamics as determined by time-resolved microwave conductivity (TRMC) measurements. We also analyzed the effect of a potassium-acetate (MAI + KAc) treatment previously developed for co-evaporated $MAPbI_3$ films on the gradient-grown $MAPbI_3$ films.[19,24] We show that the treatment does not impact the charge carrier lifetimes or trap densities but increases the effective carrier mobilities slightly. These findings provide more fundamental insight into how a gradual composition of co-evaporated $MAPbI_3$ films affects the optoelectronic properties.

EXPERIMENTAL METHODS

Preparation of the $MAPbI_3$ Films. The $MAPbI_3$ perovskite film was deposited on amorphous quartz substrates with various thicknesses by using a co-evaporation deposition method developed in previous works.[17,19,24] The substrates were attached to a rotating plate (10 rpm rotation speed) without temperature control (i.e., floating temperature), and the target to substrate distance was around 30 cm. The perovskite was deposited by co-evaporating PbI_2 powder (TCI) and MAI powder (Lumtec) in effusion sources. The chamber was first pumped down to a high vacuum condition of less than 8×10^{-6} Torr. Then, the PbI_2 source was heated at 260 °C and MAI at 100 °C, respectively. After the MAI temperature increased to >70 °C, the chamber pressure increased to $>2 \times 10^{-5}$ Torr. The total deposition time was around 20 min for the 100 nm film, 100 min for the 400 nm film, and 180 min for the 750 nm film.[17] For the treated films, the as-prepared $MAPbI_3$ perovskite film was post-treated using a 20 mM KAc and MAI (1:1 in molar ratio) mixed solution in isopropanol (IPA). The pristine film and post-treated film were annealed at 100 °C for 30 min according to the procedure previously described.[19,24]

Photoconductance Measurements. The TRMC technique was performed to investigate the photoconductance as a function of time using an excitation wavelength of 500 nm for $MAPbI_3$. With this technique, the reduction in microwave power $[\Delta P(t)/P]$ induced by the laser pulse (repetition rate 10 Hz) was related to the change in conductance $[\Delta G(t)]$ by the sensitivity factor K

$$\frac{\Delta P(t)}{P} = -K\Delta G(t) \tag{1}$$

The TRMC signal is expressed in the product of mobility $(\mu_e + \mu_h)$ and charge carrier yield φ, which was calculated from the maximum change in photoconductance ΔG_{max}

$$\varphi(\mu_e + \mu_h) = \frac{\Delta G_{max}}{F_A I_0 e \beta} \tag{2}$$

where F_A is the fraction of light absorbed by the sample at the excitation wavelength, I_0 is the laser intensity in the number of photons per unit area per pulse, e is the elementary charge, and β is the ratio of the inner dimensions of the microwave cell. The samples were placed in a sealed microwave cell inside a glovebox to ensure that they are not exposed to ambient conditions during the measurement.

Optical Characterization. Absorption spectra were recorded using a PerkinElmer Lambda 1050 spectrophotometer equipped with an integrated sphere. The samples were placed inside the sphere to measure the total fraction of reflected and transmitted light (F_{R+T}). Then, the fraction of absorbed light (F_A) was calculated by

$$F_A = 1 - F_{R+T} \tag{3}$$

Structural Characterization. X-ray photoemission spectroscopy measurements were conducted using a Thermo Fisher K-Alpha surface spectrometer with a monochromatic Al Kα X-ray beam. XPS depth profiles were collected by etching with an ionized Ar gun. Elemental quantification was performed on the basis of survey spectra from which a Shirley-type background was subtracted. This analysis is performed with the Avantage software.

XRD patterns were obtained using a Bruker D8 ADVANCE diffractometer in the Bragg−Brentano configuration using Co Kα (λ = 1.79 Å) radiation at room temperature. Temperature-dependent XRD patterns were obtained using a Bruker D8 DISCOVER diffractometer (Cu Kα, λ = 1.54 Å) in combination with an Anton Paar XRK 900 Reactor chamber. The measurements were performed in the Bragg−Brentano configuration with a variable slit size to keep the footprint on the sample constant. The temperature was stepwise changed with 5 K/min, and the measurements were performed under vacuum. The dwell time was set to 5 min.

The morphologies of the perovskite films were characterized using a scanning electron microscope (FESEM; JEJOL JSM-7600F). The perovskites were deposited on glass/FTO substrates.

Electron-dispersive spectroscopy (EDS) spectra were obtained using a scanning electron microscope (JEOL; JSM-6010LA) with a silicon drift detector.

RESULTS AND DISCUSSION

To investigate the optoelectronic properties of graded-$MAPbI_3$ films, films with different thicknesses (100, 400, and 750 nm) were deposited on quartz substrates by co-evaporation of PbI_2 and MAI according to the procedure previously described.[17,19,24] The pristine graded $MAPbI_3$ films are denoted hereafter as "untreated" films, while the graded $MAPbI_3$ films which underwent a post-deposition spin-coating treatment with an IPA solution containing KAc and MAI (MAI + KAc)[19] are denoted as "treated". Absorbance spectra of all $MAPbI_3$ films are shown in Figure S1 in the Supporting Information. Spectra of treated $MAPbI_3$ films are comparable to those of the pristine films. In the inset of Figure S1, the wavelength-dependent absorption spectra determined from the reflection and transmission spectra (Figure S2) are reported. For all samples, absorption coefficients close to 10^5 cm^{-1} at 500 nm have been found, similar to previously reported values for $MAPbI_3$.[30]

Figure 1 shows normalized XRD patterns obtained with Co Kα X-radiation for the $MAPbI_3$ films of different thicknesses made by co-evaporation. The XRD measurements were performed in the Bragg−Brentano configuration. For all films, the two main characteristic peaks of the cubic perovskite phase located at 16.6 and 33.3°[31] indicate the good crystallization of $MAPbI_3$ with a highly preferred orientation. On increasing the thickness, the peak at 14.8° attributed to

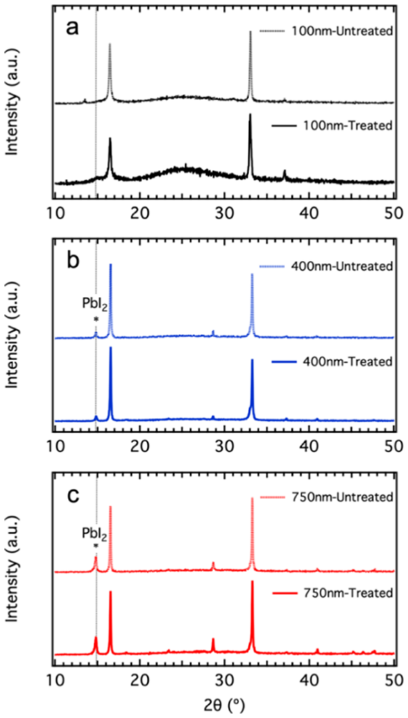

Figure 1. Normalized XRD patterns (Co Kα X-radiation) for untreated and treated co-evaporated MAPbI$_3$ films with thicknesses of 100 (a), 400 (b), and 750 nm (c). The dashed vertical line indicates the diffraction peak position of excess PbI$_2$.

PbI$_2$ is visible in the 400 nm film (Figure 1b) and becomes even more pronounced in the 750 nm MAPbI$_3$ film (Figure 1c), implying that excess PbI$_2$ is far more present in the thicker samples.[17] On the other hand, in untreated and treated MAPbI$_3$ films with an identical thickness, the amount of excess PbI$_2$ just slightly varies. It is worth noting that the compositional information of various MAPbI$_3$ thin films at different depths was measured previously using grazing incidence XRD, with incident angles varying from 0.5 to 10°.[17] These XRD patterns indicated that excess PbI$_2$ gradually decreases going from the top surfaces to the bottom in both thick MAPbI$_3$ films. This is in agreement with the low PbI$_2$ content found in the present 100 nm thick films.

In general, MAPbI$_3$ films reside at room temperature in the tetragonal phase, which is thermodynamically the most favorable phase.[32] In dry atmospheres, it is also possible that MAPbI$_3$ adopts a cubic crystal structure at room temperature using deposition by co-evaporation.[25] The absence of the (211) peak for these graded MAPbI$_3$ films prepared by co-evaporation and deposited on quartz substrates suggests that these MAPbI$_3$ films might have also a cubic phase (see Figure S3). To obtain more structural information, XRD patterns were measured by varying the temperature stepwise between 25 and 85 °C (Figure S4). Figure S4a,b shows the (200) diffraction peak of the 750 nm MAPbI$_3$ film, which shifts toward lower angles upon heating due to the thermal expansion of the lattice.[33] The (200) peak is asymmetric, with a minor contribution at lower angles (see Figure S4c), indicating the presence of some tetragonal phase. On increasing the temperature, the latter contribution becomes even smaller, which might be related to the tetragonal-to-cubic conversion. This indicates that the cubic phase coexists with the tetragonal phase in the 750 nm co-evaporated MAPbI$_3$ films on quartz at room temperature. We speculate that the excess PbI$_2$ in combination with the quartz substrate might hamper the complete conversion to the tetragonal phase. Such phase retention of MAPbI$_3$ films on quartz substrates has been reported previously.[34]

To examine the morphology and grain size in the MAPbI$_3$ films with thickness and treatment, SEM was performed, and top-view images are shown in Figure S5. In agreement with previous reports on MAPbI$_3$ films prepared by co-evaporation,[15−17,19,21,24] all MAPbI$_3$ films consist of relatively small crystalline domains (∼100 nm), forming a uniform and compact film. In a previous work,[19] we have already shown that the combined MAI and KAc treatment effectively improved the film morphology as proved by the reduced presence of pin-holes and the increased grain sizes for 750 nm films, and here, we show that this result is consistent for all three thicknesses investigated.

To obtain compositional information of the MAPbI$_3$ thin films, we performed a depth profile analysis using XPS. In Figure 2, the depth profiles of the atomic I/Pb ratio are shown for all films. The detailed atomic percentage plots of all elements in MAPbI$_3$ films are provided in the Supporting Information, Figure S6. For the 100 nm thick film, we used the average ratio in the center of the MAPbI$_3$ film yielding ratios of 2.42 and 2.32 for the untreated and treated films, respectively.

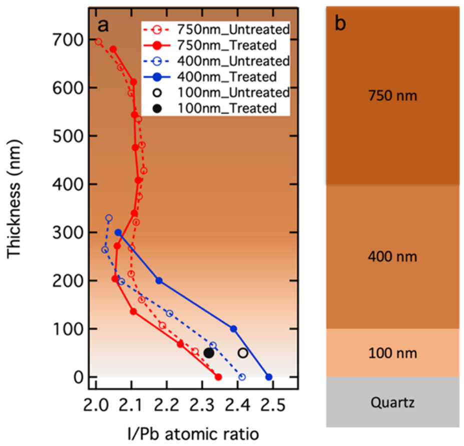

Figure 2. XPS depth profile (a). The atomic percentage ratio of I (iodine) and Pb (lead) is displayed as a function of thickness for various MAPbI$_3$ films. For 100 nm MAPbI$_3$ films, two black dots represent the average I/Pb atomic ratio of the entire 100 nm film. For the thicker MAPbI$_3$ films, the curves show the trends of the I/Pb atomic ratio evolving with the thickness during the growth of MAPbI$_3$. Note: due to the effects of surface adsorbents at the surface including, for example, oxygen, the first measurement before etching has been excluded for all films. The schematic diagram of MAPbI$_3$ films deposited on quartz with the corresponding thicknesses (b).

For both thicker films, two regimes in I/Pb ratio can be discerned. In the first 200 nm next to the quartz substrate, the I/Pb ratio reduces from about 2.4 to 2.1, implying that the MAI deficiency rises with increasing film thickness. Above 200 nm, the I/Pb ratio remains fairly constant, yielding a rather homogeneous, thick top film. Ratios below 3 indicate an MAI deficiency; however, the obtained I/Pb ratio might, to some extent, diverge from the actual ratio due to inaccuracies in the detection and analysis. Nevertheless, trends in the I/Pb atomic ratios within a single sample as well as differences in the I/Pb atomic ratios between various samples can still be compared and analyzed. In addition, trends in the I/Pb atomic ratios are consistent with XPS results previously reported, showing that I/Pb ratios at the top surface reduced from 2.7 ± 0.3 for the 100 nm $MAPbI_3$ film to 2.2 ± 0.3 for the 750 nm $MAPbI_3$ film.[17]

To confirm the elemental compositions of the $MAPbI_3$ films, we performed additional EDS. In Figure S7, the average atomic ratios of I/Pb in the entire film of 400 and 750 nm are shown to be 2.8 and 2.5, respectively. Although these values are higher than those found by XPS, the trend is similar. Moreover, the XPS and EDS results are in line with the conclusions from XRD showing an excess of PbI_2 for the 400 and 750 nm films.

As expected, the trend of the I/Pb ratio followed the background pressure during the deposition,[17] which is dominated by the partial pressure of MAI.[28] Hence, a reduction in the vacuum pressure leads to a decrease of the deposition rate of MAI, which thus results in the increasing MAI deficiency in the top part of the thick $MAPbI_3$ films.

As previously reported, an MAI deficiency or an excess of PbI_2 can lead to n-type doping of the $MAPbI_3$ film.[29,35−39] With increasing MAI deficiencies, the film becomes more n-type-doped, that is, the Fermi level increases as shown also from the ultraviolet photoelectron spectroscopy data in our previous paper.[17] Hence, we conclude that the initial part close to the substrate is less n-doped than the top part. To understand how this affects the charge carrier dynamics, we put forward a simplified band structure diagram as provided in Scheme 1 consisting of two n-type semiconductors but with different Fermi energy levels. In equilibrium, an internal electric field is formed, forcing the excess electrons to drift toward the top part, while holes drift toward the bottom region. This hypothesis implies that light-induced excess carriers will be rapidly separated by drift independent from the optical excitation side, resulting in longer charge carrier lifetimes in the thick $MAPbI_3$ films.

Scheme 1. Simplified Band Diagram of a Co-evaporated $MAPbI_3$ Film with a Gradient Composition Assuming the Top Part Is More Heavily n-Type Doped Than the Bottom Part[a]

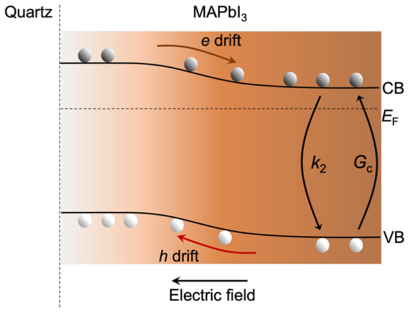

[a] On Fermi level alignment, a depletion film with an internal electric field is formed. Hence, on optical excitation, excess holes and electrons are separated by the internal electric field independent of the excitation side. G_c represents the photogeneration of charge carriers; k_2 depicts the second-order recombination rate.

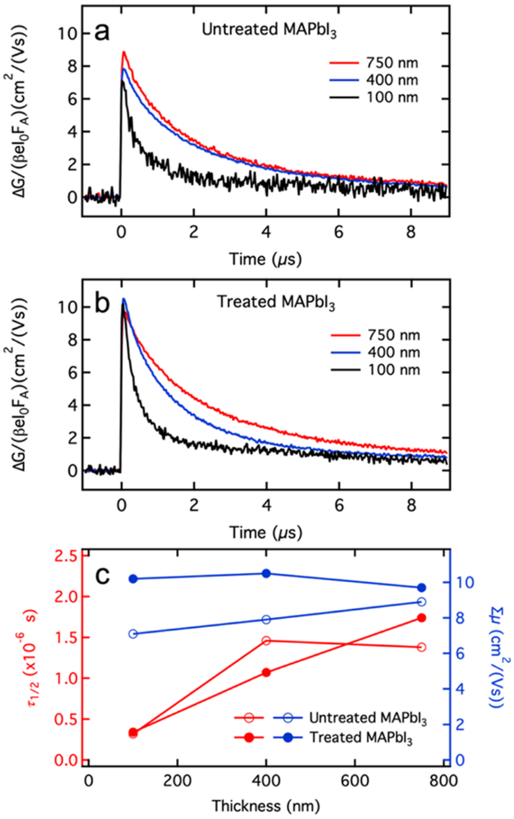

Figure 3. TRMC traces for untreated (a) and treated (b) films with the thickness of 100, 400, and 750 nm recorded on excitation at 500 nm with incident light intensities corresponding to initial charge carrier densities of 10^{14} cm^{-3} and normalized for the amount absorbed photons. In (c), the half lifetime (left axis) and mobility (right axis) extracted from TRMC traces as a function of thickness for both untreated and treated $MAPbI_3$ films are shown.

To further verify our hypothesis regarding the band diagram, we carried out TRMC experiments. Note that using this approach, we can probe excess carriers as long as they are mobile. Figure 3 shows the photoconductance traces (ΔG) normalized by the number of absorbed photons as a function of time. The initial increase of the signal originates from the generation of free charge carriers, while the decay is attributed to the immobilization of excess charge carriers via trapping or the recombination of electrons and holes. With increasing light intensity, the decay kinetics become faster, which is due to enhanced second-order electron−hole recombination (see Figure S8). More importantly, on increasing the thickness of the $MAPbI_3$ films, the lifetimes of mobile carriers become substantially longer for both untreated (Figure 3a) and treated films (Figure 3b). This is in line with the assumption that in thick $MAPbI_3$ films, the internal electric field separates the excess holes and electrons, suppressing recombination, leading to longer charge carrier lifetimes. In addition, excitation at longer wavelengths (see Figure S9), leading to a more homogeneous excitation profile within the thick perovskite layers (see Figure S11), yields similar decay kinetics, which is in agreement with our model. The decay kinetics are only slightly slower than those displayed by time-resolved photoluminescence (TRPL) (see Figure S10 and ref 19). While TRPL is only sensitive to radiative band-to-band recombination, TRMC probes carriers in the bands, providing a complementary picture of the charge carrier dynamics in perovskites, as also previously observed in a lateral perovskite homojunction.[40] For both untreated and treated films, the signal heights which are corrected for the number of absorbed photons are almost independent of the film thickness, meaning

https://doi.org/10.1021/acsaem.2c00664
ACS Appl. Energy Mater. 2022, 5, 7049−7055

that the yield and mobility for the different thicknesses are very comparable.

Figure 3c shows a 20% increase in the maximum signal height on post treatment. Given the low exciton binding energy of approximately 15 meV of $MAPbI_3$,[41] we can assume that the free charge carrier generation yield, φ, is close to unity at room temperature for $MAPbI_3$. Therefore, we conclude that the summation of electron and hole mobilities, $\Sigma\mu$, increases from ~8.5 to 11.2 $cm^2\ V^{-1}\ s^{-1}$ for the untreated and treated $MAPbI_3$, respectively. This increase in effective mobility can be related to the expanded crystal domain size, as previously shown in spin-coated films,[42] induced here by the KAc + MAI treatment.

To further study the large difference in charge carrier lifetimes, we measured the photoconductance using either front- or back-side excitation at a wavelength of 300 nm (Figure 4a). Since the penetration depth at 300 nm is less than 100 nm (see Figure S11), we can selectively excite the top (using the front side) or bottom part (using the back side) of the $MAPbI_3$ film. Previously, TRMC traces recorded with front and back illumination showed at very short timescales of tens of nanoseconds a variation in rise time, which was linked to the presence of excess PbI_2 at the top surface for the 400 and 750 nm films.[17] In Figure 4b−g, the intensity-normalized photoconductance traces of $MAPbI_3$ films recorded on excitation from both sides on 100 times' longer timescales are shown. For the 100 nm film (Figure 4b,c), the front- and back-side TRMC traces do not reveal appreciable differences in the charge carrier dynamics. This is consistent because identical regions are probed regardless of the illumination side. Interestingly, also for both thick films, overlapping TRMC traces are found for excitation from the front- and back-sides (Figure 4d−g). The negligible differences in the charge carrier lifetime in the bottom and top parts imply that in both cases, the internal electric field effectively separates the excess carriers. This means electrons are effectively pulled toward the top part, while holes drift toward the substrate side. By comparing Figure 4d with 4e and 4f with 4g, we conclude that the untreated and treated films with an identical thickness show comparable trends. This implies that it is not the post-treatment but the actual growth in film thickness during the co-evaporation deposition process that is responsible for the elongation of charge carrier lifetimes. The gradual composition as discussed above is in line with these observations. In addition, we can rule out that the $MAPbI_3$ region facing the quartz surface is of a lower quality.

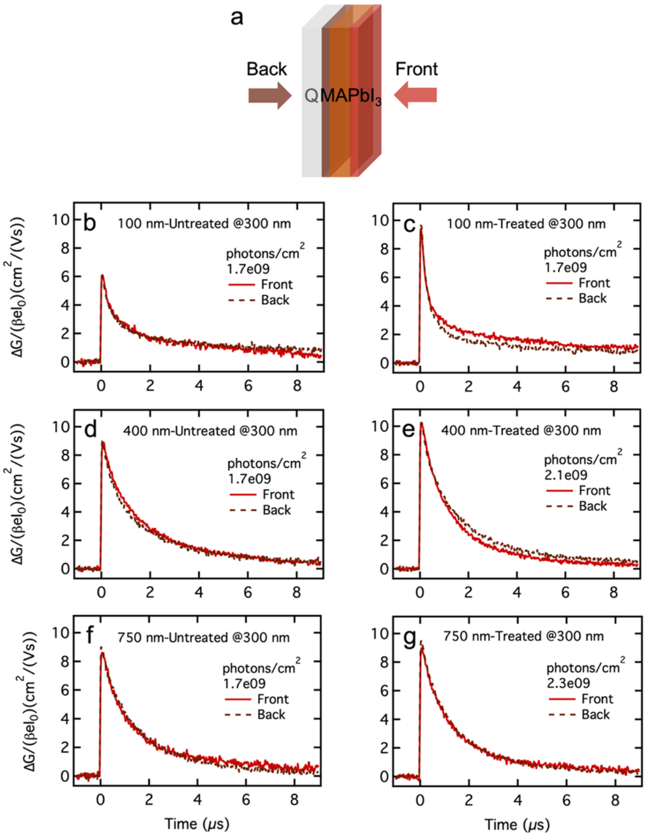

Figure 4. Schematic representation of laser illumination from the backside (Q: quartz) and front side (a). Intensity-normalized TRMC traces for (b,c) 100, (d,e) 400, and (f,g) 750 nm evaporated $MAPbI_3$ films recorded on excitation at 300 nm for front (brick red solid lines) and back (dark red dashed lines) excitation at an incident intensity of around 2×10^9 photons/cm^2/pulse. Left and right panels are for untreated and treated $MAPbI_3$, respectively.

CONCLUSIONS

In this work, the structural and optoelectronic properties of co-evaporated $MAPbI_3$ films with compositional gradients with and without potassium acetate treatment are investigated. XPS depth analysis shows that the I/Pb atomic ratio decreases with depth, indicating MAI deficiencies become more prominent with thicker films, resulting in differently n-doped regions. We suggest that on equilibration of the Fermi levels in these differently n-doped regimes, a depletion film is formed. To investigate how the band diagram affects the optoelectronic properties, TRMC was used, showing a consistent elongation of the charge carrier lifetimes with increasing thickness. This can be explained by the drift of excess carriers induced by the internal electric field, leading to physical separation and preventing rapid recombination. TRMC results on selective excitation at 300 nm prove that charge transport of holes and electrons to the top and bottom parts of the film, respectively, occurs equally well. There is no sign that the quality of the initially formed film is inferior to the top part in terms of mobility or trap state density. In addition, we observed an increase of the electron and hole mobilities by 20% when introducing the MAI + KAc treatment, which can be related to the enlarged grain size of treated $MAPbI_3$. The results from this work provide valuable insights into the optoelectronic properties of $MAPbI_3$ films with a graded composition.ﬂ

ASSOCIATED CONTENT

Supporting Information

The Supporting Information is available free of charge at https://pubs.acs.org/doi/10.1021/acsaem.2c00664.

Optical absorption, reflection and transmission spectra; temperature-dependent XRD patterns; SEM images; XPS results; EDS spectra; and detailed TRMC results (PDF)

AUTHOR INFORMATION

Corresponding Authors

Annalisa Bruno − *Energy Research Institute@NTU (ERI@N), Nanyang Technological University, 637553 Singapore,*

Singapore; orcid.org/0000-0002-6963-1682; Email: Annalisa@ntu.edu.sg

Tom J. Savenije − *Faculty of Applied Sciences, Delft University of Technology, 2629 HZ Delft, The Netherlands;* orcid.org/0000-0003-1435-9885; Email: T.J.Savenije@tudelft.nl

Authors

Jiashang Zhao − *Faculty of Applied Sciences, Delft University of Technology, 2629 HZ Delft, The Netherlands*

Jia Li − *Energy Research Institute@NTU (ERI@N), Nanyang Technological University, 637553 Singapore, Singapore*

Xiaohui Liu − *Faculty of Applied Sciences, Delft University of Technology, 2629 HZ Delft, The Netherlands*

Lars J. Bannenberg − *Faculty of Applied Sciences, Delft University of Technology, 2629 HZ Delft, The Netherlands;* orcid.org/0000-0001-8150-3694

Complete contact information is available at:
https://pubs.acs.org/10.1021/acsaem.2c00664

Notes

The authors declare no competing financial interest.

■ ACKNOWLEDGMENTS

J.Z. acknowledges the CSC (China Scholarship Council) for funding, file no. 201906360169. J.L. and A.B. acknowledge funding by the National Research Foundation, Prime Minister's Office, Singapore, under the Energy Innovation Research Program (grant nos: NRF2015EWT-EIRP003-004, Solar CRP: S18-1176-SCRP) and Intra-CREATE Collaborative grant (NRF2018-ITC001-001). Bart Boshuizen and Duco Bosma are acknowledged for providing the XPS and EDS measurements, respectively.

■ REFERENCES

(1) Kojima, A.; Teshima, K.; Shirai, Y.; Miyasaka, T. Organometal Halide Perovskites as Visible-Light Sensitizers for Photovoltaic Cells. *J. Am. Chem. Soc.* **2009**, *131*, 6050−6051.

(2) Im, J. H.; Lee, C. R.; Lee, J. W.; Park, S. W.; Park, N. G. 6.5% Efficient Perovskite Quantum-Dot-Sensitized Solar Cell. *Nanoscale* **2011**, *3*, 4088−4093.

(3) Kim, H. S.; Lee, C. R.; Im, J. H.; Lee, K. B.; Moehl, T.; Marchioro, A.; Moon, S. J.; Humphry-Baker, R.; Yum, J. H.; Moser, J. E.; Grätzel, M.; Park, N. G. Lead Iodide Perovskite Sensitized All-Solid-State Submicron Thin Film Mesoscopic Solar Cell with Efficiency Exceeding 9%. *Sci. Rep.* **2012**, *2*, 591.

(4) Heo, J. H.; Im, S. H.; Noh, J. H.; Mandal, T. N.; Lim, C.-S.; Chang, J. A.; Lee, Y. H.; Kim, H.-j.; Sarkar, A.; Nazeeruddin, M. K.; Grätzel, M.; Seok, S. I. Efficient Inorganic-Organic Hybrid Heterojunction Solar Cells Containing Perovskite Compound and Polymeric Hole Conductors. *Nat. Photonics* **2013**, *7*, 486−491.

(5) Zhou, H.; Chen, Q.; Li, G.; Luo, S.; Song, T.-b.; Duan, H.-S.; Hong, Z.; You, J.; Liu, Y.; Yang, Y. Interface Engineering of Highly Efficient Perovskite Solar Cells. *Science* **2014**, *345*, 542−546.

(6) *Best Research-Cell Efficiencies*; NREL, 2022.

(7) Stranks, S. D.; Eperon, G. E.; Grancini, G.; Menelaou, C.; Alcocer, M. J. P.; Leijtens, T.; Herz, L. M.; Petrozza, A.; Snaith, H. J. Electron-Hole Diffusion Lengths Exceeding 1 Micrometer in an Organometal Trihalide Perovskite Absorber. *Science* **2013**, *342*, 341−344.

(8) Shi, D.; Adinolfi, V.; Comin, R.; Yuan, M.; Alarousu, E.; Buin, A.; Chen, Y.; Hoogland, S.; Rothenberger, A.; Katsiev, K.; Losovyj, Y.; Zhang, X.; Dowben, P. A.; Mohammed, O. F.; Sargent, E. H.; Bakr, O. M. Low Trap-State Density and Long Carrier Diffusion in Organolead Trihalide Perovskite Single Crystals. *Science* **2015**, *347*, 519−522.

(9) Wei, H.; Fang, Y.; Mulligan, P.; Chuirazzi, W.; Fang, H.-H.; Wang, C.; Ecker, B. R.; Gao, Y.; Loi, M. A.; Cao, L.; Huang, J. Sensitive X-Ray Detectors Made of Methylammonium Lead Tribromide Perovskite Single Crystals. *Nat. Photonics* **2016**, *10*, 333−339.

(10) Cho, H.; Jeong, S.-H.; Park, M.-H.; Kim, Y.-H.; Wolf, C.; Lee, C.-L.; Heo, J. H.; Sadhanala, A.; Myoung, N.; Yoo, S.; Im, S. H.; Friend, R. H.; Lee, T.-W. Overcoming the Electroluminescence Efficiency Limitations of Perovskite Light-Emitting Diodes. *Science* **2015**, *350*, 1222−1225.

(11) Gu, C.; Lee, J.-S. Flexible Hybrid Organic−Inorganic Perovskite Memory. *ACS Nano* **2016**, *10*, 5413−5418.

(12) Liu, M.; Johnston, M. B.; Snaith, H. J. Efficient Planar Heterojunction Perovskite Solar Cells by Vapour Deposition. *Nature* **2013**, *501*, 395−398.

(13) Gil-Escrig, L.; Dreessen, C.; Palazon, F.; Hawash, Z.; Moons, E.; Albrecht, S.; Sessolo, M.; Bolink, H. J. Efficient Wide-Bandgap Mixed-Cation and Mixed-Halide Perovskite Solar Cells by Vacuum Deposition. *ACS Energy Lett.* **2021**, *6*, 827−836.

(14) Klipfel, N.; Momblona, C.; Kanda, H.; Shibayama, N.; Nakamura, Y.; Mensi, M. D.; Liu, C.; Roldán-Carmona, C.; Nazeeruddin, M. K. Crystallographically Oriented Hybrid Perovskites via Thermal Vacuum Codeposition. *Sol. RRL* **2021**, *5*, 2100191.

(15) Hutter, E. M.; Sutton, R. J.; Chandrashekar, S.; Abdi-Jalebi, M.; Stranks, S. D.; Snaith, H. J.; Savenije, T. J. Vapour-Deposited Cesium Lead Iodide Perovskites: Microsecond Charge Carrier Lifetimes and Enhanced Photovoltaic Performance. *ACS Energy Lett.* **2017**, *2*, 1901−1908.

(16) Vaynzof, Y. The Future of Perovskite Photovoltaics—Thermal Evaporation or Solution Processing? *Adv. Energy Mater.* **2020**, *10*, 2003073.

(17) Li, J.; Dewi, H. A.; Wang, H.; Zhao, J.; Tiwari, N.; Yantara, N.; Malinauskas, T.; Getautis, V.; Savenije, T. J.; Mathews, N.; Mhaisalkar, S.; Bruno, A. Co-Evaporated MAPbI3 with Graded Fermi Levels Enables Highly Performing , Scalable , and Flexible p-i-n Perovskite Solar Cells. *Adv. Funct. Mater.* **2021**, *31*, 2103252.

(18) Werner, J.; Sahli, F.; Fu, F.; Diaz Leon, J. J.; Walter, A.; Kamino, B. A.; Niesen, B.; Nicolay, S.; Jeangros, Q.; Ballif, C. Perovskite/Perovskite/Silicon Monolithic Triple-Junction Solar Cells with a Fully Textured Design. *ACS Energy Lett.* **2018**, *3*, 2052−2058.

(19) Li, J.; Wang, H.; Chin, X. Y.; Dewi, H. A.; Vergeer, K.; Goh, T. W.; Lim, J. W. M.; Lew, J. H.; Loh, K. P.; Soci, C.; Sum, T. C.; Bolink, H. J.; Mathews, N.; Mhaisalkar, S.; Bruno, A. Highly Efficient Thermally Co-Evaporated Perovskite Solar Cells and Mini-Modules. *Joule* **2020**, *4*, 1035−1053.

(20) Roß, M.; Gil-Escrig, L.; Al-Ashouri, A.; Tockhorn, P.; Jošt, M.; Rech, B.; Albrecht, S. Co-Evaporated p-i-n Perovskite Solar Cells beyond 20% Efficiency: Impact of Substrate Temperature and Hole-Transport Layer. *ACS Appl. Mater. Interfaces* **2020**, *12*, 39261−39272.

(21) Dewi, H. A.; Li, J.; Wang, H.; Chaudhary, B.; Mathews, N.; Mhaisalkar, S.; Bruno, A. Excellent Intrinsic Long-Term Thermal Stability of Co-Evaporated MAPbI3 Solar Cells at 85 °C. *Adv. Funct. Mater.* **2021**, *31*, 2100557.

(22) Erdenebileg, E.; Wang, H.; Li, J.; Singh, N.; Dewi, H. A.; Tiwari, N.; Mathews, N.; Mhaisalkar, S.; Bruno, A. Low-Temperature Atomic Layer Deposited Electron Transport Layers for Co-Evaporated Perovskite Solar Cells. *Sol. RRL* **2022**, *6*, 2100842.

(23) Li, J.; Dewi, H. A.; Wang, H.; Lew, J. H.; Mathews, N.; Mhaisalkar, S.; Bruno, A. Design of Perovskite Thermally Co-Evaporated Highly Efficient Mini-Modules with High Geometrical Fill Factors. *Sol. RRL* **2020**, *4*, 2000473.

(24) Li, J.; Wang, H.; Dewi, H. A.; Mathews, N.; Mhaisalkar, S.; Bruno, A. Potassium Acetate-Based Treatment for Thermally Co-Evaporated Perovskite Solar Cells. *Coatings* **2020**, *10*, 1163.

(25) Palazon, F.; Pérez-del-Rey, D.; Dänekamp, B.; Dreessen, C.; Sessolo, M.; Boix, P. P.; Bolink, H. J. Room-Temperature Cubic Phase Crystallization and High Stability of Vacuum-Deposited Methylammonium Lead Triiodide Thin Films for High-Efficiency Solar Cells. *Adv. Mater.* **2019**, *31*, 1902692.

(26) Klein, M.; Li, J.; Bruno, A.; Soci, C. Co-Evaporated Perovskite Light-Emitting Transistor Operating at Room Temperature. *Adv. Electron. Mater.* **2021**, *7*, 2100403.

(27) Maddalena, F.; Chin, X. Y.; Cortecchia, D.; Bruno, A.; Soci, C. Brightness Enhancement in Pulsed-Operated Perovskite Light-Emitting Transistors. *ACS Appl. Mater. Interfaces* **2018**, *10*, 37316−37325.

(28) Abzieher, T.; Feeney, T.; Schackmar, F.; Donie, Y. J.; Hossain, I. M.; Schwenzer, J. A.; Hellmann, T.; Mayer, T.; Powalla, M.; Paetzold, U. W. From Groundwork to Efficient Solar Cells: On the Importance of the Substrate Material in Co-Evaporated Perovskite Solar Cells. *Adv. Funct. Mater.* **2021**, *31*, 2104482.

(29) Emara, J.; Schnier, T.; Pourdavoud, N.; Riedl, T.; Meerholz, K.; Olthof, S. Impact of Film Stoichiometry on the Ionization Energy and Electronic Structure of CH3NH3PbI3 Perovskites. *Adv. Mater.* **2016**, *28*, 553−559.

(30) Hutter, E. M. *Revealing the Fate of Photo-Generated Charges in Metal Halide Perovskites*; Delft University of Technology, 2018.

(31) Hutter, E. M.; Eperon, G. E.; Stranks, S. D.; Savenije, T. J. Charge Carriers in Planar and Meso-Structured Organic–Inorganic Perovskites: Mobilities, Lifetimes, and Concentrations of Trap States. *J. Phys. Chem. Lett.* **2015**, *6*, 3082−3090.

(32) Poglitsch, A.; Weber, D. Dynamic Disorder in Methylammoniumtrihalogenoplumbates (II) Observed by Millimeter-Wave Spectroscopy. *J. Chem. Phys.* **1987**, *87*, 6373−6378.

(33) Jacobsson, T. J.; Schwan, L. J.; Ottosson, M.; Hagfeldt, A.; Edvinsson, T. Determination of Thermal Expansion Coefficients and Locating the Temperature-Induced Phase Transition in Methylammonium Lead Perovskites Using X-Ray Diffraction. *Inorg. Chem.* **2015**, *54*, 10678−10685.

(34) Osherov, A.; Hutter, E. M.; Galkowski, K.; Brenes, R.; Maude, D. K.; Nicholas, R. J.; Plochocka, P.; Bulović, V.; Savenije, T. J.; Stranks, S. D. The Impact of Phase Retention on the Structural and Optoelectronic Properties of Metal Halide Perovskites. *Adv. Mater.* **2016**, *28*, 10757−10763.

(35) Wang, Q.; Shao, Y.; Xie, H.; Lyu, L.; Liu, X.; Gao, Y.; Huang, J. Qualifying Composition Dependent p and n Self-Doping in CH3NH3PbI3. *Appl. Phys. Lett.* **2014**, *105*, 163508.

(36) Dänekamp, B.; Müller, C.; Sendner, M.; Boix, P. P.; Sessolo, M.; Lovrincic, R.; Bolink, H. J. Perovskite-Perovskite Homojunctions via Compositional Doping. *J. Phys. Chem. Lett.* **2018**, *9*, 2770−2775.

(37) Cui, P.; Wei, D.; Ji, J.; Huang, H.; Jia, E.; Dou, S.; Wang, T.; Wang, W.; Li, M. Planar p−n Homojunction Perovskite Solar Cells with Efficiency Exceeding 21.3. *Nat. Energy* **2019**, *4*, 150−159.

(38) Fassl, P.; Zakharko, Y.; Falk, L. M.; Goetz, K. P.; Paulus, F.; Taylor, A. D.; Zaumseil, J.; Vaynzof, Y. Effect of Density of Surface Defects on Photoluminescence Properties in MAPbI3 Perovskite Films. *J. Mater. Chem. C* **2019**, *7*, 5285−5292.

(39) Euvrard, J.; Yan, Y.; Mitzi, D. B. Electrical Doping in Halide Perovskites. *Nat. Rev. Mater.* **2021**, *6*, 531−549.

(40) Lin, Y.; Li, T.; Liu, Y.; Bahrami, B.; Guo, D.; Fang, Y.; Shao, Y.; Chowdhury, A. H.; Wang, Q.; Deng, Y.; Gruverman, A.; Savenije, T. J.; Qiao, Q.; Huang, J. Perovskite Solar Cells with Embedded Homojunction via Nonuniform Metal Ion Doping. *Cell Rep. Phys. Sci.* **2021**, *2*, 100415.

(41) Miyata, A.; Mitioglu, A.; Plochocka, P.; Portugall, O.; Wang, J. T.-W.; Stranks, S. D.; Snaith, H. J.; Nicholas, R. J. Direct Measurement of the Exciton Binding Energy and Effective Masses for Charge Carriers in Organic-Inorganic Tri-Halide Perovskites. *Nat. Phys.* **2015**, *11*, 582−587.

(42) Reid, O. G.; Yang, M.; Kopidakis, N.; Zhu, K.; Rumbles, G. Grain-Size-Limited Mobility in Methylammonium Lead Iodide Perovskite Thin Films. *ACS Energy Lett.* **2016**, *1*, 561−565.